



ELSEVIER

Contents lists available at [SciVerse ScienceDirect](http://www.sciencedirect.com)

Continental Shelf Research

journal homepage: www.elsevier.com/locate/csr

Research papers

Tidal eddy motions in the western Gulf of Maine, Part 2:
Secondary flow

G.M. Marques*, W.S. Brown

School for Marine Science and Technology, University of Massachusetts Dartmouth, 706 South Rodney French Boulevard, New Bedford, MA 02744, USA

ARTICLE INFO

Article history:

Received 31 March 2011

Received in revised form

15 January 2012

Accepted 15 February 2012

Available online 23 February 2012

Keywords:

Tidal eddy motion

Secondary circulation

Coriolis effects

Upwelling

ABSTRACT

The kinematics and dynamics of the tidal circulation in the western Gulf of Maine (GoM) region are investigated with focus on the secondary circulation. This study is motivated by previous research suggesting the formation and evolution of transient tidal eddy motions in a high-density scallop region off Chatham, MA. Three-dimensional flow velocity and surface elevation fields were obtained using the QUODDY finite-element coastal ocean circulation model in the barotropic mode and forced by the five most important tidal constituents in the region (M_2 , N_2 , S_2 , K_1 and O_1). The secondary flow kinematics related to the primary tidal flows feature time/space-varying convergences and divergences that are affected by the associated transient tidal eddy motions. Interestingly, the upwelling and downwelling in the study region were not dominated by the secondary circulation. Rather, the model results show that instantaneous vertical motions close to the coast and close to the bathymetric slope are mainly controlled by the divergence/convergence of the primary flow. The instantaneous secondary flow dynamics are mainly controlled by a balance between pressure gradient and Coriolis forces. Off Chatham, the surface maximum strength of the secondary flow calculated by the model is consistent with theoretical predictions of 0.025 m/s. The mechanisms controlling the long-term average tidal secondary circulation, which is relevant for biological transport, are discussed.

© 2012 Elsevier Ltd. All rights reserved.

1. Introduction

The Great South Channel (GSC) region in the western Gulf of Maine (GoM; Fig. 1) is characterized by prominent eddy motion activity that is directly coupled with tidal motion (Brown et al., submitted for publication). This region is a critical area of sea scallop recruitment (Stokesbury and Harris, 2004), and understanding its physical processes would help to improve management of this resource.

It has long been known that three-dimensional secondary flows around coastal promontories result in physical and biological fronts (Wolanski and Hamncr, 1988). Field observations and numerical simulations have confirmed the presence of secondary flow patterns near coastal promontories (Pingree, 1978; Geyer, 1993; Wolanski et al., 1996; Alae et al., 2004; Doglioli et al., 2004; Berthot and Pattiaratchi, 2006; Neill et al., 2007; Vennell and Old, 2007; White and Wolanski, 2008). The secondary flow results from a local imbalance between either the vertically varying centrifugal or Coriolis forces and the cross-stream pressure gradient force. The first balance always drives the near-bottom flow towards the inside of the bend and the near-

surface flow outward, while in the second one the direction of the secondary flow depends on the direction of the main flow. These two mechanisms reinforce the strength of the secondary flow for cyclonic curvature, while they compete with each other for anticyclonic curvature. The maximum strength of the secondary flow has been derived under centrifugal and Coriolis effects (Alae et al., 2004), with good agreement with observed velocities (Alae et al., 2004; Berthot and Pattiaratchi, 2006).

Garrett and Loucks (1976) suggested that the centrifugal force associated with the strong tidal current was responsible for driving upwelling along the Yarmouth shore of Nova Scotia. From a long-term perspective, they compared the strength of Coriolis and centrifugal forces and found that the latter was greater by a factor of two. Tidal current data in the vicinity of Gay Head, USA, reported by Geyer (1993), clearly showed the presence of secondary flow. The observed secondary flow corresponded to 15–20% of the observed main flow.

Many studies (Geyer, 1993; Berthot and Pattiaratchi, 2006; Neill et al., 2007; Vennell and Old, 2007; White and Wolanski, 2008) have suggested that upwelling occurs in the presence of transient tidal eddies as a result of centrifugal-induced secondary flow. Only Pingree (1978) and Doglioli et al. (2004) have reported the occurrence of upwelling in the presence of Coriolis-induced (i.e., $R_{om} \sim 1$ and $R_{om} < 1$, respectively) secondary flow around such geological features.

* Corresponding author. Now at: Rosenstiel School of Marine and Atmospheric Science, Meteorological and Physical Oceanography, 4600 Rickenbacker Causeway, Miami, FL 33149, USA.

E-mail address: gmarques@umassd.edu (G.M. Marques).

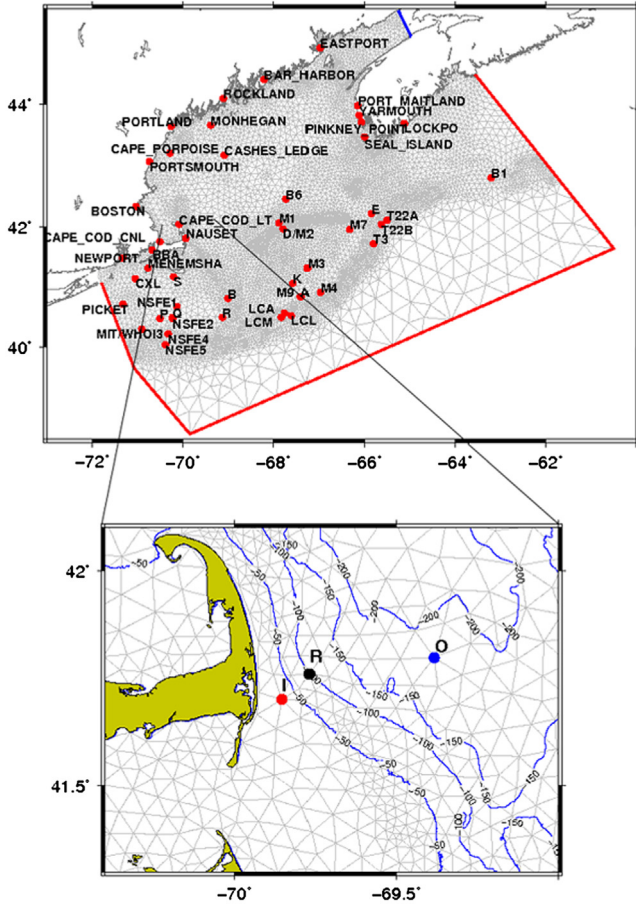


Fig. 1. (Top) The location of the study area in the western Gulf of Maine and the Holboke (1998) GHS mesh for the QUODDY model domain. The observed sites (Moody et al., 1984) used for the model-observation comparison studies are also shown. (Bottom) The Great South Channel study region showing the mesh resolution, the bathymetric contours and the locations of the reference node (R), in black, and the nodes (I and O) at which time series of elevation, velocity, vorticity and the terms in Eqs. (8) and (9) are presented.

This paper is a continuation of our previous work on the primary structure of the transient tidal eddy motions in the western GoM (Brown et al., submitted for publication). Using measurements we have shown that this region is dominated by the semidiurnal tides, with M_2 being the most important constituent in terms of both currents and sea-surface elevation. Additionally, the hydrographic survey revealed well-mixed winter conditions. We concluded that the primary flow (eddy motion) is the result of the interaction between the tidal forcing and the complex topography (rather than the coastal promontory itself). Here, the kinematics and dynamics of the tidal circulation are investigated, with focus on the induced secondary flow. The paper's objectives are to (1) describe the instantaneous and long-term three-dimensional velocity structure within the study area and (2) identify their generation mechanisms. In contrast to some of the previous studies on three-dimensional secondary flows around coastal promontories (Geyer, 1993; Wolanski et al., 1996; Berthot and Pattiaratchi, 2006; Neill et al., 2007; Vennell and Old, 2007; White and Wolanski, 2008), we show that the instantaneous secondary flow in our study region is the result of the streamwise flow being turned by the Coriolis force. This is the effect of a reduction in the centrifugal force due to the relatively larger (in comparison with the above mentioned studies) radius of flow curvature, which is controlled by the local topography. On the other hand, the long-term (31-day average) results indicate that centrifugally induced secondary flows are responsible for

driving upwelling along most parts of the study region. The latter is consistent with the case investigated by Garrett and Loucks (1976).

The remainder of the paper is organized as follows: first, a brief review of the physical mechanisms responsible for controlling the secondary flow is presented in Section 2. A description of the numerical model QUODDY is given in Section 3. Results are presented in Section 4, followed by a discussion in Section 5. Finally, the principal findings and future directions are summarized in Section 6.

2. Theoretical considerations

To study the secondary flow, Kalkwijk and Booij (1986) and others (Geyer, 1993; Hench and Leutlich, 2003; Alaei et al., 2004) have adopted a streamwise/normal coordinate system because it allows for a more intuitive physical interpretation of strongly curving flow fields. In this coordinate frame, the streamwise coordinate s is defined to be in the direction of the vertically-averaged flow everywhere, while the normal (or cross-stream) coordinate n is positive to the left of the vertically-averaged flow. The z -axis is positive upward. By definition, the vertically varying normal velocity u_n is the secondary circulation and the vertically averaged normal flow \bar{u}_n is zero everywhere.

The Kalkwijk and Booij (1986) model for secondary flow is based on the assumptions of $u_s \gg u_n$, uniform density, and negligible vertical advection. The approximate normal direction momentum equation is

$$\frac{\partial u_n}{\partial t} + u_s \frac{\partial u_n}{\partial s} - \frac{u_s^2}{Rs} + fu_s + g \frac{\partial \eta}{\partial n} - \frac{\partial}{\partial z} \left(A \frac{\partial u_n}{\partial z} \right) = 0, \quad (1)$$

where A is the eddy viscosity, f is the Coriolis force, η is the water level, g is the acceleration of gravity, and Rs is the radius of curvature of the streamline (defined to be positive for clockwise curvature). The depth average of Eq. (1) is

$$u_s \frac{\partial \bar{u}_n}{\partial s} - \frac{\bar{u}_s^2}{Rs} + f \bar{u}_s + g \frac{\partial \eta}{\partial n} + \frac{\tau_n}{\rho h} = 0, \quad (2)$$

where h is the water depth and τ_n is the bottom friction in the normal direction given by

$$\frac{\tau_n}{\rho} = \left[A \frac{\partial u_n}{\partial z} \right]_{z=-h}. \quad (3)$$

Kalkwijk and Booij (1986) subtracted (1) and (2) and neglected the depth-averaged streamwise advection term in (2), which tends to be small, leading to the following expression for the secondary circulation:

$$\underbrace{\frac{\partial u_n}{\partial t}}_{(a)} + u_s \underbrace{\frac{\partial u_n}{\partial s}}_{(b)} - \frac{\partial}{\partial z} \underbrace{\left(A \frac{\partial u_n}{\partial z} \right)}_{(c)} - \frac{\tau_n}{\rho h} = - \underbrace{\frac{u_s^2 - \bar{u}_s^2}{Rs}}_{(e)} - \underbrace{f(u_s - \bar{u}_s)}_{(f)}. \quad (4)$$

(Note that normal water level gradient $\partial \eta / \partial n$ does not appear.)

The terms on the left-hand side (LHS) of Eq. (4) are: (a) the local acceleration of the normal velocity, (b) streamwise advection, (c) internal friction of the secondary circulation, (d) bottom friction. The two driving forces on the right-hand side (RHS) of Eq. (4), which arise from departures of the streamwise velocity from its vertical mean, are: the depth-dependent (e) centrifugal and (f) Coriolis forces. Kalkwijk and Booij (1986) solved Eq. (4) analytically for the cases of Coriolis-induced and curvature-induced circulation by assuming steady state, a logarithmic velocity profile in the vertical, and a parabolic form for the eddy viscosity.

The observations by Geyer (1993) indicate that the Kalkwijk and Booij (1986) model may not be applicable to oceanic

conditions such as those at Gay Head and similar sites. Geyer (1993) found that Kalkwijk and Booij (1986) u_n values for the Gay Head situation were up to four times lower than those observed for the tidal flow at that location. He suggested that both enhanced shears in the observed streamwise flow and reduced vertical mixing due to stratification were responsible for the discrepancy. However, according to Alae et al. (2004), for curved oscillatory oceanic flows, such as tidal flows around promontories, the time-dependent term and, more importantly, the varying characteristics of the flow in the streamwise direction, both neglected in Kalkwijk and Booij (1986), may have contributed to the discrepancy.

Based on Geyer's (1993) results, Alae et al. (2004) proposed a model in which the nonlinear (b) plays a key role, while internal friction (c) could be neglected when compared to bottom friction (d).

By further assuming steady state (term $a=0$), the Alae et al. (2004) form of Eq. (4) becomes:

$$u_s \frac{\partial u_n}{\partial s} - \frac{\tau_n}{\rho h} = \frac{u_s^2 - \bar{u}_s^2}{R_s} - f(u_s - \bar{u}_s). \tag{5}$$

The Alae et al. (2004) nondimensionalization of Eq. (5) yielded a nondimensional modified Rossby number $R_{om} \sim 2u_s / fR_s$, and an equivalent Reynolds number $R_{ef} \sim H/C_D b$, where b is the streamwise length scale. The former quantifies the relative importance of centrifugal and Coriolis forces, while the latter quantifies the relative importance of advection versus friction.

Alae et al. (2004) defined four secondary flow regimes in terms of these two numbers (Fig. 2). They also estimated the surface maximum strengths of the secondary flow u_n for each flow regime using numerical model simulations. Berthot and Pattiaratchi (2006) used the Alae et al. (2004) model to study the three-dimensional structure of a headland-associated sandbank near Cape Leveillain (Shark Bay, Western Australia). Their predicted result for the surface maximum normal velocity ($u_n=24$ cm/s), balanced by inertial and centrifugal forces, was in accordance with the normal flow velocities measured at Cape Leveillain (surface flow up to 25 cm/s). In Section 5.1, we show that in our study site the normal direction balance is between friction and Coriolis forces (regime A proposed by Alae et al., 2004). This balance is the result of the local topography gradients and a reduction in the centrifugal force due to the large radius of flow curvature. The maximum normal velocity computed using Alae

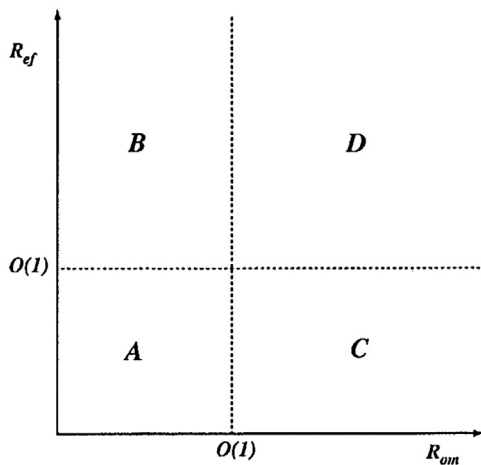


Fig. 2. The flow regime diagram based upon the two nondimensional numbers, R_{om} and R_{ef} (Alae et al., 2004).

Table 1

Times in hours selected for analysis from Fig. 3 and their designated letters.

Time (h)	Letter	Time (h)	Letter
0	A	6.5	E
1.9	B	8.5	F
3.1	C	9.7	G
4.4	D	10.9	H

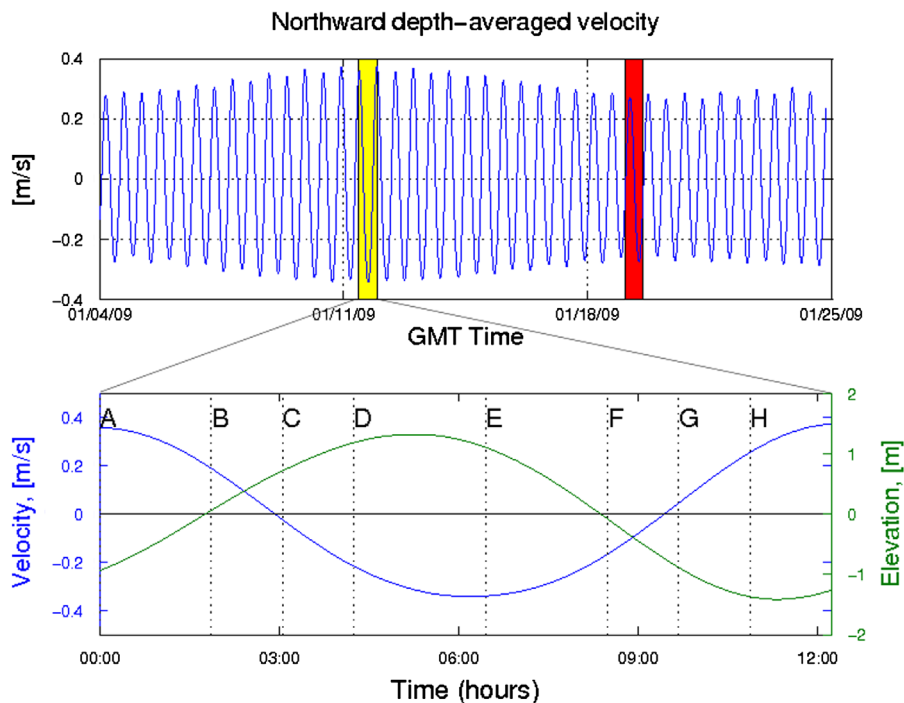


Fig. 3. (Top) Northward depth-averaged velocity time series at the reference model node (R located in Fig. 1). The spring and neap phases are highlighted by yellow and red, respectively. (bottom) The times selected for analysis, which represent spring tides conditions, are indicated with letters A–H (see also Table 1).

et al. (2004) method is in agreement with our numerical results (see Section 5.2).

3. Numerical model

3.1. Model description

The three-dimensional, nonlinear, prognostic, f-plane, finite-element coastal ocean circulation model named QUODDY was used (Lynch et al., 1996). This model uses the Mellor–Yamada level 2.5 turbulent closure model (MY25) in the vertical with a linearized partial-slip condition enforced at the bottom. The model was run in the barotropic mode, in which water properties are homogeneous. The use of this mode is justified by the well-mixed winter conditions observed in the region (Brown et al., submitted for publication). The QUODDY model mesh used here was defined by the Holboke (1998) GHSD mesh (Fig. 1). The resolution of this mesh varies from about 10 km in the gulf to about 5 km near the coastlines (i.e., around Cape Cod) with even finer resolution (1.5 km) in the regions of steep bathymetric slopes, like the north flank of Georges Bank. A 10-m minimum depth was adopted for the coastal boundary elements. Twenty-one (21) sigma layers are used in the vertical. In this application, a velocity shear dependent method (Smagorinsky, 1963) is used to calculate horizontal viscosity. The model assumes that bottom flow $\mathbf{u} = \sqrt{u^2 + v^2}$ is subject to quadratic bottom boundary stress, according to $C_d |\mathbf{u}| \mathbf{u}$, where the time/space constant bottom drag coefficient C_d used here is 0.005. The latter was selected because our model verification work (Brown et al., submitted for publication) showed this value provided good agreement with observed tidal constituents derived from Moody et al. (1984).

3.2. Numerical model forcing and operation

Three principal semidiurnal (M_2 , N_2 and S_2) and two principal diurnal (K_1 and O_1) tidal elevations were used to force QUODDY at the deep ocean and western cross-shelf sections (Fig. 1). These tidal-forcing elevations were calculated using the EastCoast 2001 tidal harmonics database by Mukai et al. (2002), which was based on a harmonic analysis of the ADVanced CIRCulation (ADCIRC) finite element hydrodynamic numerical model simulations. Normal flow boundary conditions were used along boundaries in Bay of Fundy section (see blue line in Fig. 1). The normal boundary flows for the M_2 , M_4 , M_6 , N_2 , S_2 , K_1 and O_1 tidal constituents were calculated using a 3-D linear, finite-element, diagnostic numerical model FUNDY6 (Lynch et al., 1992), using the GHSD mesh (Fig. 1) with the same elevation forcing at the open ocean boundaries.

The model was spun up for the first six M_2 tidal cycles and then run for two months between December 2008 and January 2009; a time step of 21.83 s was used in this application and the results were saved every 10.18 min. These model results were analyzed in the dynamical framework that is outlined next.

3.3. Depth-averaged momentum budgets

Following Hench and Leutlich (2003), we employ the shallow water, depth-averaged x – y momentum Eqs. (6) and (7) in which the horizontal diffusion terms (which tend to be much smaller than the other terms) were omitted

$$\frac{\partial \bar{u}}{\partial t} + \bar{u} \frac{\partial \bar{u}}{\partial x} + \bar{v} \frac{\partial \bar{u}}{\partial y} - f \bar{v} + g \frac{\partial \eta}{\partial x} + \frac{(C_D \sqrt{u^2 + v^2}) \bar{u}}{H} = 0, \quad (6)$$

$$\frac{\partial \bar{v}}{\partial t} + \bar{u} \frac{\partial \bar{v}}{\partial x} + \bar{v} \frac{\partial \bar{v}}{\partial y} + f \bar{u} + g \frac{\partial \eta}{\partial y} + \frac{(C_D \sqrt{u^2 + v^2}) \bar{v}}{H} = 0, \quad (7)$$

where \bar{u} and \bar{v} are depth-averaged velocity components in the x and y direction, respectively, g is the acceleration due to gravity, f is Coriolis parameter, η is the surface elevation, C_D is the bottom friction coefficient and H is the total water depth ($H = h + \eta$).

Eqs. (6) and (7) were then rotated into a streamwise-normal (s – n) coordinate system, where a complete description of this coordinate transformation can be found in Hench and Leutlich (2003). The resulting s – n momentum equations are

$$\frac{\overbrace{\frac{\partial \bar{u}_s}{\partial t}}^{(g)}} + \overbrace{\bar{u}_s \frac{\partial \bar{u}_s}{\partial s}}^{(h)} + g \frac{\overbrace{\frac{\partial \eta}{\partial s}}^{(i)}}{\partial s} + \frac{\overbrace{C_D \bar{u}_s^2}}{H} = 0, \quad (8)$$

$$\overbrace{\bar{u}_s \frac{\partial \alpha}{\partial t}}^{(k)} + \frac{\overbrace{\bar{u}_s^2}}{R_s} + \overbrace{f \bar{u}_s}^{(m)} + g \frac{\overbrace{\frac{\partial \eta}{\partial n}}^{(n)}}{\partial n} = 0, \quad (9)$$

where $\bar{u}_s(x, y, t)$ is the streamwise velocity, $\alpha(x, y, t)$ is the angle between the local streamwise flow vector and the positive x axis,

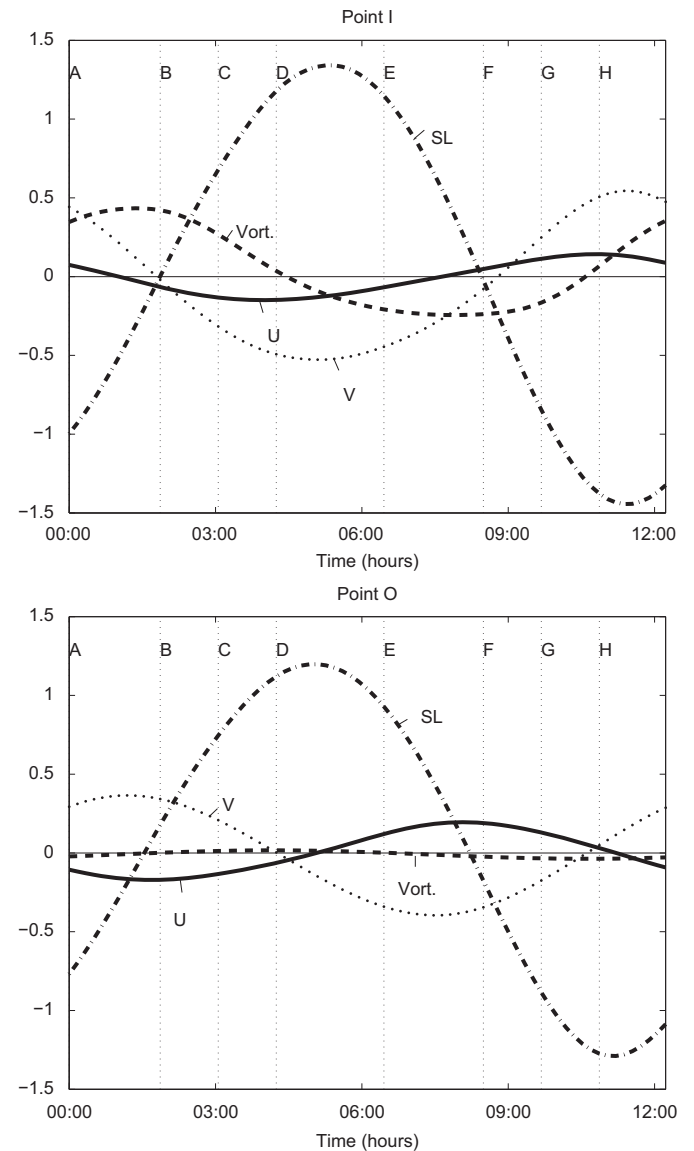


Fig. 4. Model-derived time series at the inshore point I (top) and offshore point O (bottom) located in Fig. 1. Shown are the sea-surface elevation (SL in m, dash-dot), depth-averaged northward (alongshore) velocity (V in m/s, dotted), depth-averaged eastward (cross-shore) velocity (U in m/s, solid), and relative vorticity (Vort in 10^{-4} s^{-1} , dashed).

and $R_s(x,y,t)$ is the radius of streamwise flow curvature. In the streamwise momentum Eq. (8), (g) is the local streamwise acceleration, (h) is the streamwise advective (or Bernoulli) acceleration, (i) is the streamwise pressure gradient, (j) is the nonlinear bottom friction. In the normal momentum Eq. (9), (k) is the local rotary acceleration, (l) is the centrifugal force, (m) is the Coriolis force and (n) is the normal-direction pressure gradient.

The model x - y velocity and elevation fields in the unstructured grid were used to construct the momentum terms in Eqs. (8) and (9) at each computational node. The local acceleration terms were treated with a forward-Euler finite difference scheme. The conservation of momentum was estimated at each node based on the ratio between the sum of the terms (g–j) in Eq. (8), and (k–n) in Eq. (9) and the sum of the absolute values of these terms. We found that momentum was conserved (typically to within 1%) at all grid points in both the x and y directions, as well as the s and n directions.

To provide a more physically intuitive picture of the momentum balances, the time series results in the following subsections are presented in terms of momentum fluxes (obtained by multiplying each term of Eqs. (8) and (9) by the instantaneous full water depth H , where $H = \eta + h$).

4. Results

The time series results presented here pertain to spring tide conditions (see Fig. 3 and Table 1). Fig. 1 indicates the location of the reference node (R) used to define the phase of the tide, and

the location of the nodes used in the time series analysis (points I and O). Point I is located off Chatham, MA, inside the coastal boundary layer (CBL) where the eddy motion is formed. Point O, is located away from the CBL in a region less influenced by the eddy motion. We focus on selected times (indicated by letters A–H and detailed in Table 1) during the semidiurnal tidal cycle considered.

4.1. Time series at fixed locations

4.1.1. Kinematics

In this section, the kinematics of the flow in terms of time series of sea surface elevation, velocity and relative vorticity are contrasted for sites I and O (see Fig. 4).

At the nearshore site (I), sinusoidal sea surface elevation and northward velocity time series (Fig. 4top) are approximately 180° out of phase; kinematics that are consistent with those of a progressive tidal wave. The relative vorticity is approximately in quadrature and noticeably asymmetrical, indicating nonlinearity effects. These results show that relative vorticity associated with the anti-clockwise (ACW) eddy motion, that is generated during the flood cycle, is approximately $2 \times 10^{-5} \text{ s}^{-1}$ stronger than that associated with the clockwise (CW) eddy motion generated during the ebb cycle. Brown et al. (submitted for publication) have shown that ACW and CW eddy motions are associated with the maximum and minimum relative vorticity near point I, respectively.

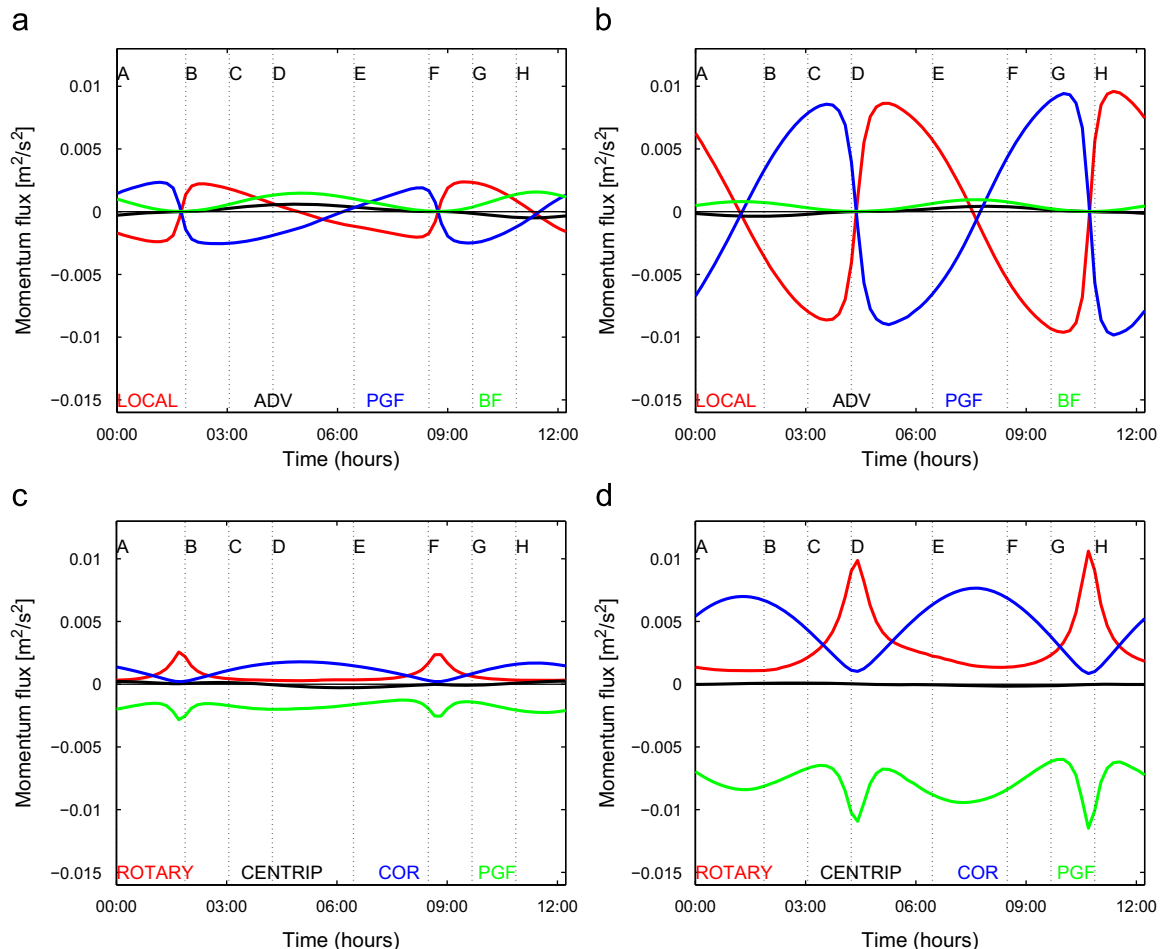


Fig. 5. Momentum flux terms at nodes (left) I and (right) O (located in Fig. 1). The streamwise direction terms (top) are: local (red), advective (black), pressure gradient (blue) and bottom friction (green); the normal direction terms (bottom) are: rotary (red), centripetal (black), Coriolis (blue) and pressure gradient (green). These terms are defined in Eqs. (8) and (9). (a) Streamwise dir. Point I; (b) streamwise dir. Point O; (c) normal dir. Point I; and (d) normal dir. Point O.

At the offshore site (O) the sea surface elevation, velocity, and a very weak ($O 10^{-6} s^{-1}$) relative vorticity are sinusoidal (Fig. 4bottom). At this location, the sea surface elevation and northward velocity are approximately 90° out of phase, a near standing tidal wave kinematics.

4.1.2. Dynamics

Here we focus on time series of the s – n momentum terms, in Eqs. (8) and (9), derived from sites (I) and (O).

At the nearshore site (I), the predominant streamwise momentum balance (Fig. 5a) is between local acceleration (term d) and pressure gradient force (term f), with an important contribution from bottom friction (term g) during strong flood/ebb. In the normal direction (Fig. 5c), the predominant momentum balance is between Coriolis and pressure gradient forces (i.e., geostrophy). Many of the streamwise and normal momentum terms exhibit considerable asymmetry. For example, the streamwise adverse (i.e., positive) pressure gradient generated after maximum flood is higher than the counterpart generated after maximum ebb. Interestingly, at the times of eddy motion formation (i.e., flow separation) the terms in the streamwise direction tend to instantaneously vanish (Fig. 5a). At the same time, in the normal direction, rotary acceleration (term h) and pressure gradient (term k) become stronger, and Coriolis force weaker (Fig. 5c).

At the offshore site (O), the predominant streamwise momentum balance is between local acceleration (term d) and pressure

gradient (term f) (Fig. 5b). In the normal direction, the primary balance is between Coriolis force (term j) and pressure gradient force (term k), except during the change of tides, when the balance is between pressure gradient force and rotary acceleration (term h) (Fig. 5d). The momentum terms time series in the streamwise (Fig. 5b) and normal (Fig. 5d) directions exhibit a stronger symmetry when compared to site (I) (note the change in scale).

4.2. Three-dimensional velocity structure

In the following subsections we examine the three-dimensional velocity structure at times of maximum flood flow, in the presence of an ACW eddy motion, during maximum ebb flow, and finally in the presence of a CW eddy motion (letters A, C, E and G, respectively, in Fig. 3).

4.2.1. Maximum flood flow (A)

At maximum flood (time A in Fig. 3), the depth-averaged flow normal to the reference transect (red line in Fig. 6a) is curving in an ACW sense and there is an onshore pressure gradient force along the transect. The streamwise flow through the transect shows strongest vertical shear in the shallower nearshore region, with some along transect variation (Fig. 6b).

The normal velocity pattern along the transect is consistent with an ACW deep water cell next to a CW shallow cell, with surface convergence near the bathymetry break (Fig. 6c). There is

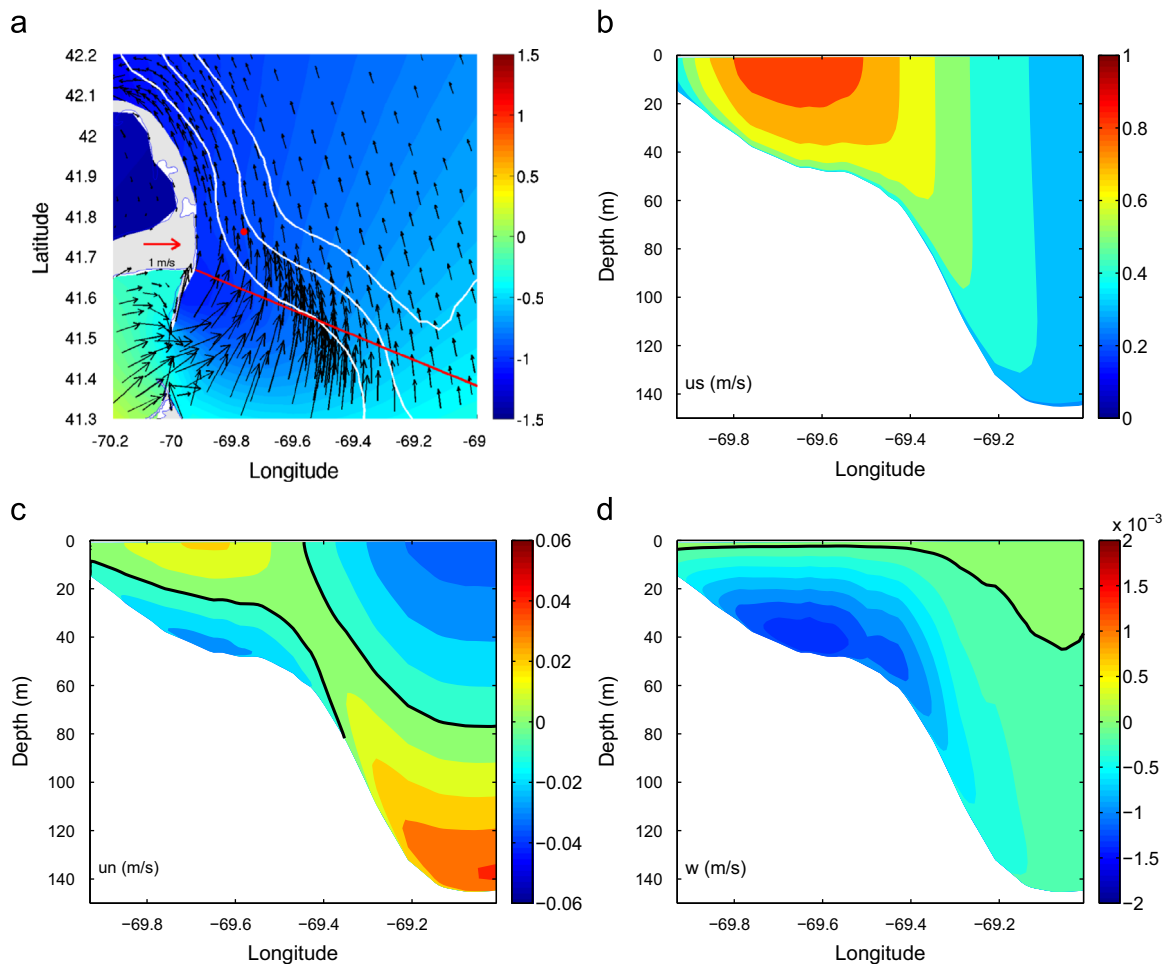


Fig. 6. Model variable distributions at the time of maximum flood (time A) at the reference node R (red dot) in terms of: (a) depth-averaged velocity (m/s) and color-coded sea-surface elevation (SSE, m), in which the reference transect (red line) and the 50-, 100- and 150-m isobaths are shown; (b) streamwise velocity (m/s); (c) normal or secondary flow velocity (m/s), where positive values means away from the coast; and (d) vertical velocity (m/s). The black lines in (c) and (d) indicate the zero contour value. (a) Depth-ave. vel. (m/s) and SSE (m); (b) streamwise velocity (m/s); (c) normal velocity (m/s); and (c) vertical velocity (m/s).

downwelling in the region of the bathymetry break and shoreward (Fig. 6d). The depth-averaged velocity divergence pattern in the region of the transect, which is consistent within the 21 model layers, is illustrated in Fig. 7a. Thus at maximum flood, the depth-averaged velocity convergence seems to be consistent with the occurrence of downwelling near the coast (Fig. 6d). Therefore, (a) close to the coast downwelling appears to be controlled by the main flow and not by the normal velocity, (b) while at the bathymetry break it appears to be controlled by both main flow and normal velocity.

4.2.2. Transition to ebb flow (C)

During first half ebb (time C in Fig. 3), an ACW eddy motion (that developed near the coast at time B) is evident in the depth-averaged flow (Fig. 8a). The sea surface elevation field indicates a general regional southward pressure gradient force. The streamwise flow transect pattern shows the lateral gradients associated with the eddy motion (Fig. 8b).

The nearshore normal velocity pattern observed during maximum flood (Fig. 6c) has moved offshore (Fig. 8c). Just one CW cell is observed, connected by a wide band of upwelling near the coast (Fig. 8d). As shown in Fig. 7b, this coastal upwelling is also supported by the positive values of the depth-averaged velocity divergence. Although the normal flow is toward the same direction in both these regions, the streamwise flow converges offshore (Fig. 7b), resulting in downwelling (Fig. 8d). The strength of the vertical velocity (~ 0.5 mm/s) is smaller than those during maximum flood.

4.2.3. Maximum ebb flow (E)

At maximum ebb (time E in Fig. 3), the depth-averaged flow is curving in a CW sense (Fig. 9a), and there is an offshore pressure gradient force along the transect. Again, the streamwise flow along the reference transect shows a modest amount of vertical shear in the shallow region and a strong horizontal variation (Fig. 9b). However, this horizontal variation is weaker than that observed during maximum flood.

The normal velocity along the transect shows a double cell pattern in opposite sense to that at maximum flood, with an ACW shallow water cell and a CW deep cell (Fig. 9c). The bathymetry break region divides these two different regions, with flow converging at the bottom and diverging at the surface, resulting in upwelling (Fig. 9d). The maximum strength in the vertical velocity (up to 1.5 mm/s) occurs close to the bottom in the depth range of 30–60 m. As shown in Fig. 7c, the positive values of the depth-averaged velocity divergence along the reference transect suggest that the coastal upwelling is controlled by the streamwise flow.

4.2.4. Transition to flood flow (G)

During first half flood (time G in Fig. 3), a CW eddy motion (that developed near the coast between times F and G) is evident in the depth-averaged flow (Fig. 10a). The sea surface elevation field indicates a general regional northward pressure gradient force. Like during the presence of an ACW eddy motion, the streamwise flow transect pattern shows horizontal variation associated with the eddy motion (Fig. 10b).

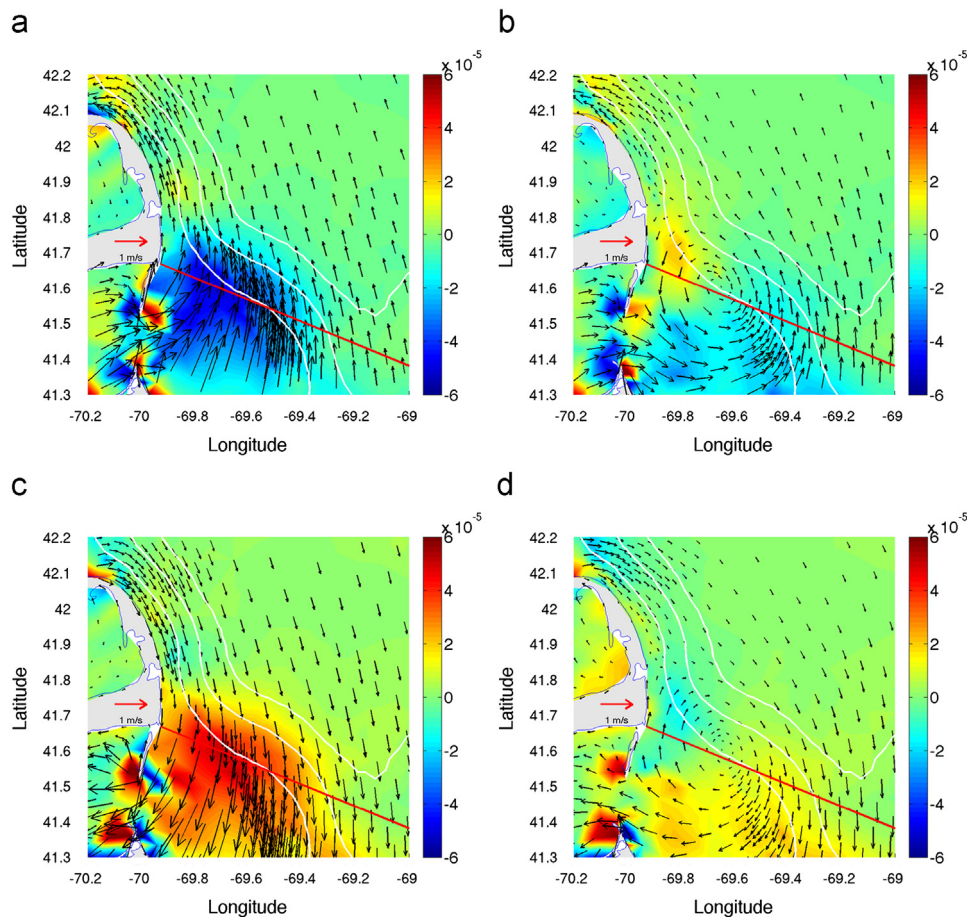


Fig. 7. Depth-averaged velocity (m/s) and its color coded divergence (s^{-1}) during (a) maximum flood, time A; (b) transition to ebb, time C; (c) maximum ebb, time E; and (d) transition to flood, time G. The reference section location (red line) and the 50-, 100- and 150-m isobaths (white lines) are shown.

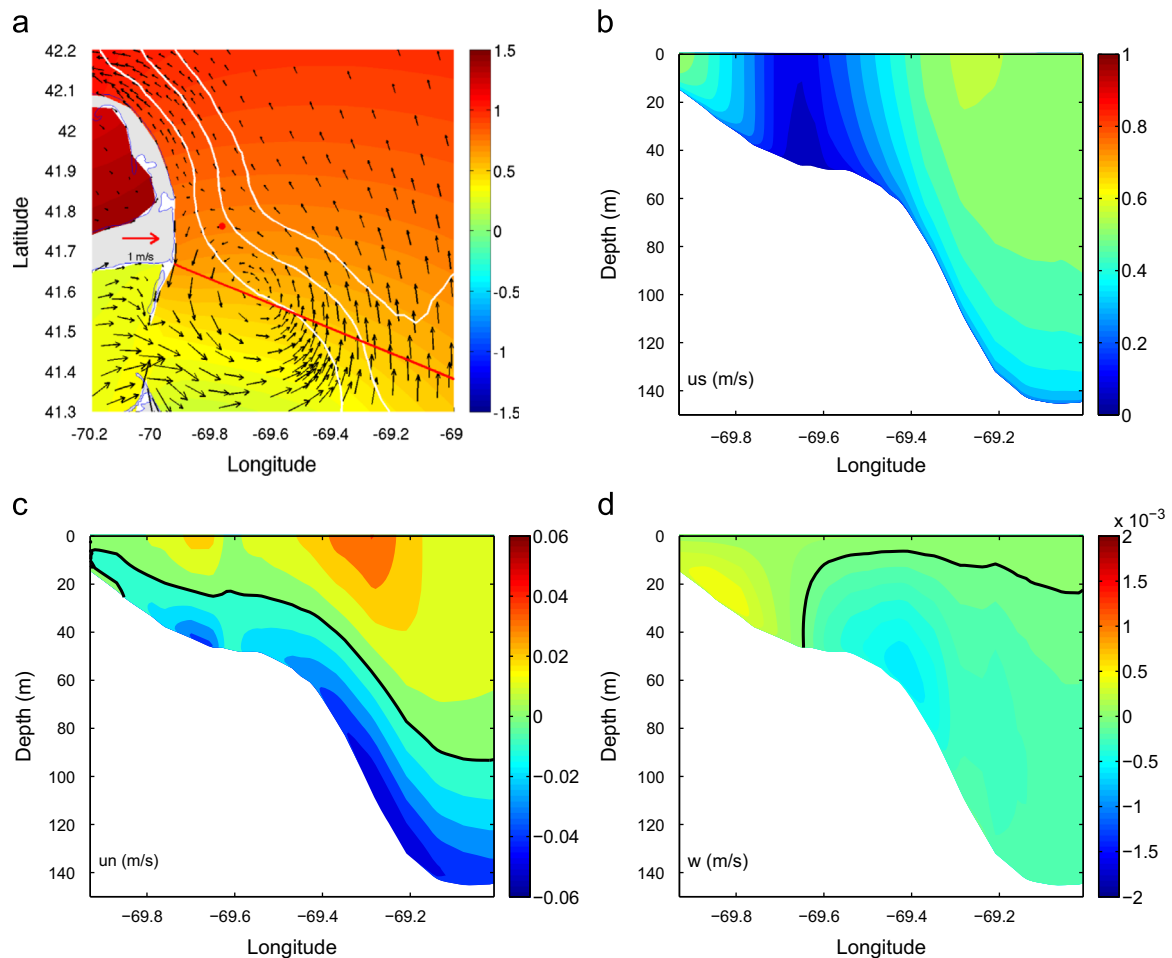


Fig. 8. As in Fig. 6, but for transition to ebb flow (time C), when an anticlockwise eddy motion is present. (a) Depth-ave. vel. (m/s) and SSE (m); (b) streamwise velocity (m/s); (c) normal velocity (m/s); and (d) vertical velocity (m/s).

The nearshore normal velocity pattern observed during maximum ebb (Fig. 9c) has moved offshore, and one ACW cell is present along the transect (Fig. 10c). This pattern is in opposite sense to that during the transition to ebb flow (Fig. 8c). The nearshore downwelling and offshore upwelling (Fig. 10d) also oppose the pattern observed in the presence of an ACW eddy motion, but their magnitudes seems smaller. Again, the strength of the vertical velocity (~ 0.4 mm/s) are smaller when compared to those during maximum ebb.

4.3. Long term average residual flow structure

The long-term, namely 31-day average, residual tidal flow is explored at the two transects depicted in Fig. 11. The reference transect 1, along which the eddy motion forms and translates, is located off the “elbow” of Cape Cod; while transect 2 is located off the northern reach of Cape Cod, where the isobaths tend to be parallel to the coastline.

The depth-averaged residual circulation pattern (Fig. 11) in the region of the reference transect 1 has a well defined ACW circulation. At the nearshore end of the reference transect 1, the residual velocities are approximately southward (ranging from 7 to 10 cm/s) and consistent with both the moored-TTE residual currents (Brown et al., submitted for publication) and the residual currents measured by Chen et al. (1995) during late spring. This result is consistent with (1) relatively stronger ACW eddy motion and (2) the idea that the residual currents over the shallower sides of the GSC are mainly due to tidal rectification (Lynch and Naimie, 1992; Chen et al., 1995).

The residual secondary flow distribution along the reference transect 1 (Fig. 12a) shows offshore residual flow in the upper layer above 40 m, and onshore flow in the lower layer. Combined with the correspondent residual vertical panel (Fig. 12c), these results suggest a single CW overturning cell. The opposite occurs for the residual secondary flow in waters shallower than 40 m (i.e., ACW overturning cell). Although this shallow circulation pattern is not closed by the residual vertical flow. Interestingly, the nearshore residual upwelling values are as large as 6.0 m/day, while the offshore values over the slope are about 4.3 m/day (Fig. 12c). Weak residual downwelling is seen in the extreme eastern region of the reference transect 1.

The residual secondary flow along the reference transect 2 shows a double cell pattern, with CW overturning in the shallower region and a weaker ACW overturning in the deeper region (Fig. 12b). These circulation cells are closed by the residual vertical flow (Fig. 12d). The intensity of the vertical residual velocities in the reference transect 2 is one order of magnitude smaller than those in transect 1.

5. Discussion

5.1. Mechanisms controlling the secondary flow

Garrett and Loucks (1976), Kalkwijk and Booij (1986) and Geyer (1993) have shown that the secondary circulation induced by centrifugal force is always directed offshore near the surface

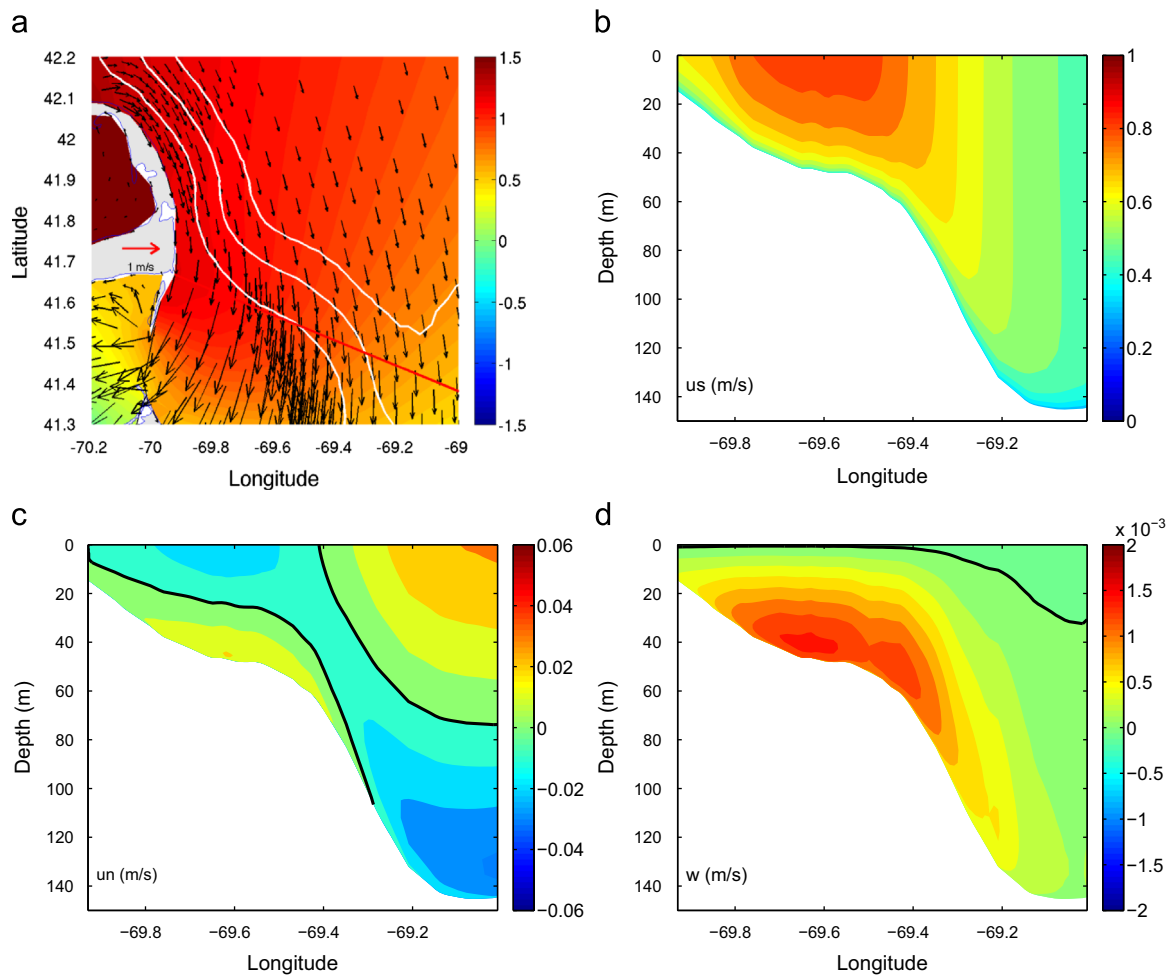


Fig. 9. As in Fig. 6, but for maximum ebb (time E). (a) Depth-ave. vel. (m/s) and SSE (m); (b) streamwise velocity (m/s); (c) normal velocity (m/s); and (d) vertical velocity (m/s).

and onshore near the bottom, independent of the streamwise flow direction. The numerical model results show that the directions of the near-bottom and near-surface secondary flow change during the M_2 tidal cycle. Therefore, we conclude that the secondary circulation in our study region is the result of the streamwise flow being turned by the Coriolis force. This conclusion is supported by depth-averaged normal-direction momentum balances in which Coriolis dominates over centrifugal forces during the tidal cycle (see Fig. 5). This balance is the result of a reduction in the centrifugal force due to the large radius of flow curvature in the region, where the latter is controlled by the local topography.

Our numerical results indicate that the secondary flow is more intense in the presence of ACW flow. For example, during maximum flood and in the presence of an ACW eddy motion (see Figs. 6c and 8c, respectively), our secondary flow is up to 2 cm/s stronger than it is during maximum ebb and in the presence of a CW eddy motion (see Figs. 9c and 10c, respectively). Concerning large-scale flows, in the regions of coastal promontories, Pingree (1978) proposed that the Coriolis force becomes important, acting with or against the centrifugal force depending upon flow direction. In such cases, the intensity of the secondary flow is amplified in ACW and reduced in CW flows (Neill et al., 2007).

As explained by Geyer (1993), vertical stratification can enhance the secondary circulation. Additionally, horizontal density gradients can influence the strength of the flow due to the thermal-wind

relation and, therefore, potentially modify the dynamics described here. These effects are expected to be important during summertime, and further investigation is required in order to describe the kinematics and dynamics in such conditions.

5.2. Secondary flow strength

The strength of the secondary flow is estimated using the Alaei et al. (2004) method in terms of $R_{ef} = h/C_d b$ and $R_{om} = 2U_s/fR_s$ (see Section 2). Using representative numerical model values during maximum flood (time A) including $U_s = 0.8$ m/s, $h = 50$ m, $b = 2 \times 10^4$ m (streamwise length scale), $R_s = 10^5$ m, $f = 9.7 \times 10^{-5}$ s $^{-1}$ and $C_d = 0.005$, we get $R_{ef} = 0.5$ and $R_{om} = 0.2$. Thus our secondary flow is the Alaei et al. (2004) regime A. Using the correspondent equation for this regime (Alaei et al., 2004, Eq. 17), we obtain $u_n = 0.025$ m/s, which compares favorably with our numerical model surface layer at 50 m depth in Fig. 6b. The maximum surface strength of the secondary circulation is approximately 3% of the instantaneous corresponding streamwise tidal flow. This number is much smaller than the percentage found in other studies where the instantaneous u_n is controlled by the centrifugal force (Geyer, 1993; Berthot and Pattiaratchi, 2006; Neill et al., 2007). This result suggests that the Alaei et al. (2004) method is reasonable in predicting the maximum surface strength of the secondary circulation off Chatham, MA.

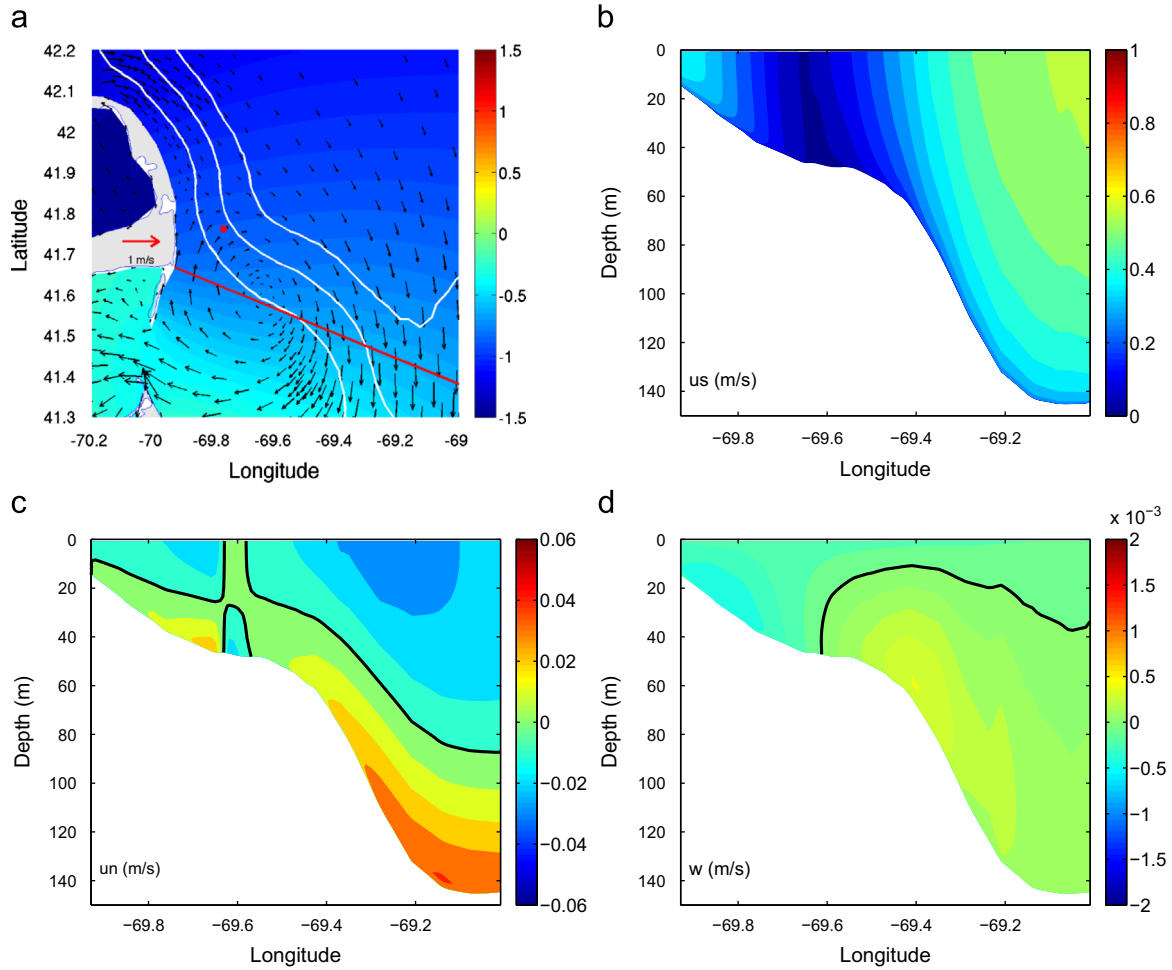


Fig. 10. As in Fig. 6, but for transition to flood flow (time G), when a clockwise eddy motion is present. (a) Depth-ave. vel. (m/s) and SSE (m); (b) streamwise velocity (m/s); (c) normal velocity (m/s); and (d) vertical velocity (m/s).

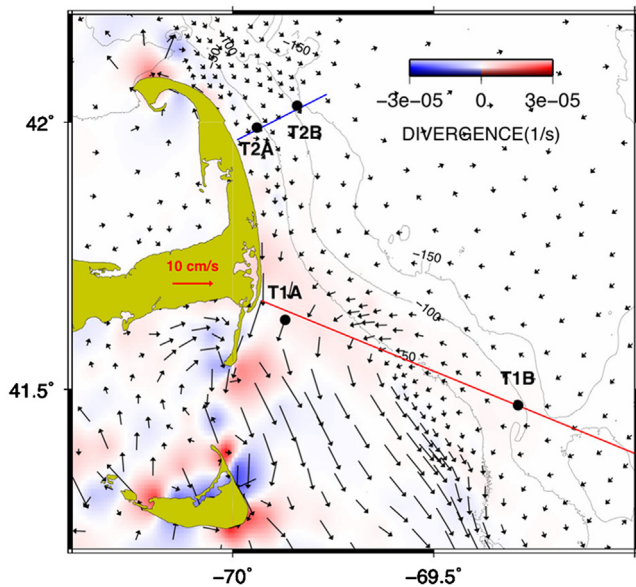


Fig. 11. Distribution of long-term depth-averaged model flow vectors (cm/s) with flow divergence (s^{-1} , red) and convergence (s^{-1} , blue). The reference transect 1 (red) and transect 2 (blue) are located; along with the nodes where both Coriolis and centrifugal forces strengths are estimated.

5.3. Upwelling and downwelling

In our study, we found that during maximum flood/ebb (times A and E in Fig. 3) the vertical velocities along the reference transect 1 are not controlled by the divergence of the secondary flow (Figs. 6 and 9). This can be shown quantitatively by using the conservation of mass equation: $\partial u_s / \partial s + \partial u_n / \partial n = -w/h$. Using the divergence of the depth-averaged streamwise flow ($\partial \bar{u}_s / \partial s$) as a proxy for the divergence of the streamwise flow ($\partial u_s / \partial s$) and assuming that $\partial u_n / \partial n = 0$, then $w = -h \partial \bar{u}_s / \partial s$. From Fig. 7a, $\partial \bar{u}_s / \partial s \sim \partial u_s / \partial s \sim -2 \times 10^{-5} s^{-1}$ for transect 1, where $h = -50$, and $w \sim -1 \times 10^{-3} m/s$. This compares favorably with the range of values in Fig. 6d. The same reasoning applies during maximum ebb. In contrast to previous results in the literature (Alaee et al., 2004; White and Wolanski, 2008), the nearshore downwelling (upwelling) during maximum flood (ebb) results from the convergence (divergence) of the main (streamwise) tidal flow. Vertical water motion in the absence of eddies has been reported for many three-dimensional numerical studies (Alaee et al., 2004; Doglioli et al., 2004; Jones et al., 2006; White and Wolanski, 2008).

5.4. Tidal long-term circulation

Following Garrett and Loucks (1976), we compare the strength of the model Coriolis (fU) and centrifugal ($\frac{1}{2}U^2/R_s$) forces, where U

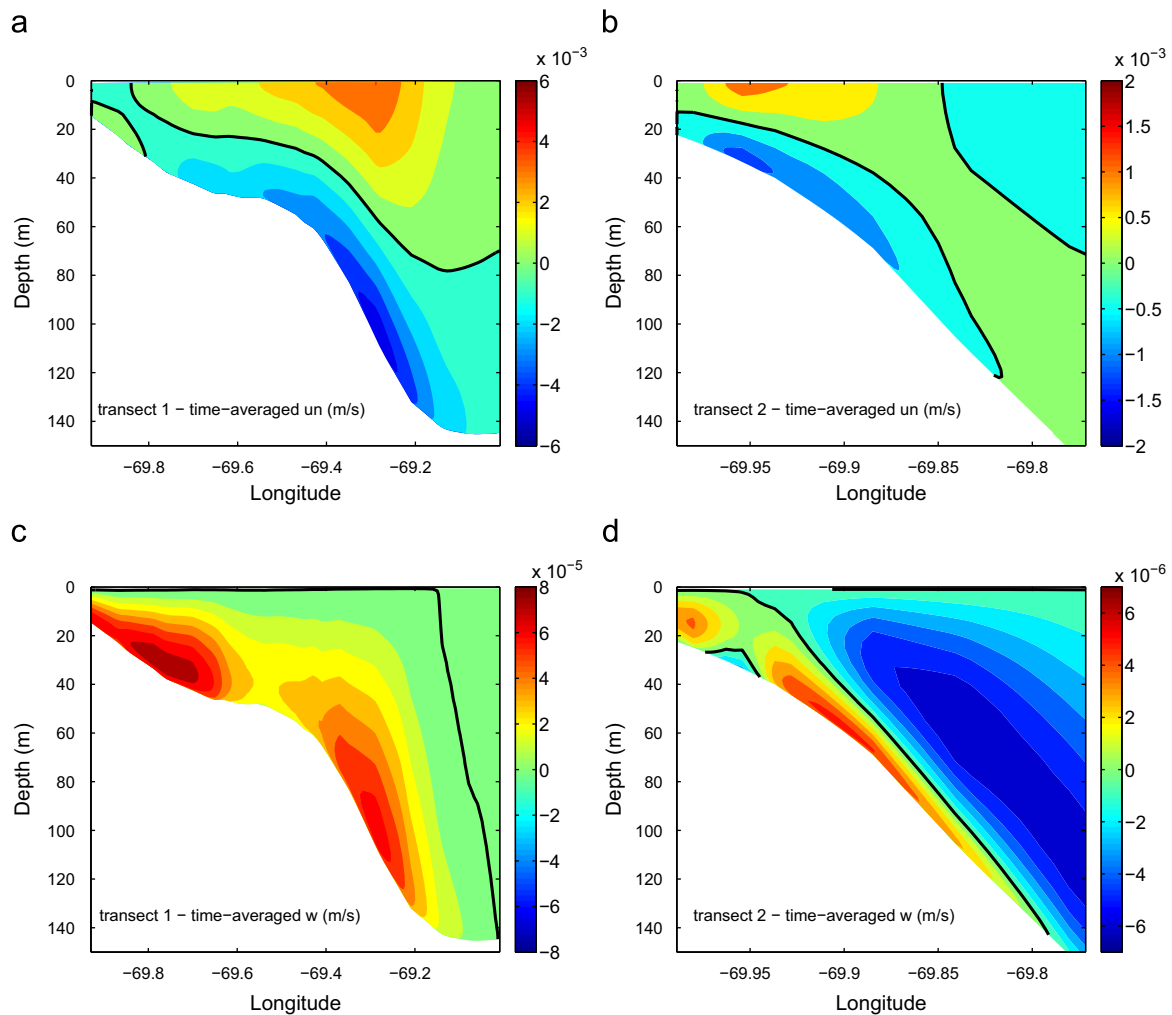


Fig. 12. The 31-day time-averaged model residual results in streamwise/normal coordinates including: (a) residual normal velocity, u_n (m/s), along the reference transect 1; (b) as (a) for transect 2; (c) residual vertical velocity, w (m/s), along reference transect 1; and (d) as (b) for reference transect 2. The zero contour lines are highlighted for clarity.

is the long-term average current, f the Coriolis parameter, U_t is the maximum tidal current magnitude and R_s its corresponding radius of flow curvature. We focus on the secondary circulation on reference transect 1, where the asymmetry in the strength of the eddy motions is most clear (Fig. 11). The nearshore long-term secondary flow pattern suggests that Coriolis force is more important than centrifugal force (Fig. 12c). Using the numerical model results for the inshore node highlighted in black (see Fig. 11), we estimate Coriolis force = $5.8 \times 10^{-6} \text{ m/s}^2$ and centrifugal force = $1.6 \times 10^{-6} \text{ m/s}^2$. Based on the streamwise direction of the flow presented in Fig. 11, the two forces are in opposition. Therefore, the small difference between them justifies the weak Coriolis force induced long-term secondary circulation nearshore (Fig. 12a). In the offshore region, the long-term secondary flow pattern indicates that centrifugal force dominates. This conclusion is supported by numerical model results which were extracted from the offshore node (see Fig. 11): Coriolis force = $2.9 \times 10^{-6} \text{ m/s}^2$ versus centrifugal force = $2.8 \times 10^{-5} \text{ m/s}^2$. The centrifugal force induced long-term secondary circulation in the deeper region is one order of magnitude larger than the Coriolis force induced circulation in the shallower region. As a result, upwelling occurs in the boundary between these two long-term secondary circulation cells (Fig. 12c).

6. Summary and conclusions

The kinematics and dynamics of the tidal flow in the western Gulf of Maine were investigated, with focus on the secondary circulation, using a validated application of the three-dimensional nonlinear hydrodynamic finite element numerical model, QUODDY. The model was forced with the five most important tidal constituents for the region (M_2 , N_2 , S_2 , K_1 and O_1) and operated in the barotropic mode.

Using model-derived results, two-dimensional momentum balance calculations in a streamwise/normal coordinate system were performed to evaluate the overall momentum balance in the representative (nearshore and offshore) regions. In the nearshore region, the spatial distribution of the momentum terms during maximum flood/ebb show the presence of a streamwise adverse pressure gradient force off Chatham, MA, and strong bottom friction, resulting in flow separation and eddy motion formation. The shallower-water kinematic characteristics are close to those of a progressive wave, where the principal streamwise dynamical balance is between pressure gradient force (PGF) and local acceleration (LA), with strong influence from bottom friction (BF) during times of significant currents. In deeper waters, the kinematic characteristics are close to those of a standing wave, where the principal streamwise dynamical balance is between

PGF and LA. For both nearshore and offshore regions, the principal normal direction dynamical balance is between PGF and Coriolis force.

A possible mechanism for the instantaneous secondary circulation computed during one M_2 tidal cycle is suggested by a local imbalance between the normal pressure gradient and Coriolis force. Our results and the case studied by Pingree (1978) and Doglioli et al. (2004) are among the few examples of Coriolis-induced ($R_{om} \sim 1$ and $R_{om} < 1$, respectively) secondary circulation in the literature. The similarity between these sites is their large radius of streamwise flow curvature ($R_s \geq \bar{u}_s/f$), which is controlled by the topography rather than the promontory itself. Interestingly, the upwelling/downwelling in our study region were not dominated by the secondary circulation. Rather, the model results show that instantaneous vertical motions close to the coast and close to the bathymetric slope are mainly controlled by the divergence/convergence of the main flow. This work is not aimed at quantifying the contribution of the streamwise flow to the vertical velocity, and further work should include that. The model result suggests that the method proposed by Alae et al. (2004) predicts reasonably well the surface maximum strength of the secondary circulation off Chatham, MA.

The long-term (31-day average) model results indicated that centrifugally induced inshore near-bottom transport dominates in most parts of the study region, resulting in nearshore upwelling. We have not discussed here the effects of wind and of horizontal and vertical density gradients on the secondary circulation. These effects are expected to be important during summer conditions, and they clearly require further investigation.

Acknowledgments

This research was supported by MIT Sea Grant, project number 2007-R/RC-104, and by NOAA Grant NA07NOS4730221 to Rutgers University through a subcontract to UMassD. We are grateful to Frank “Chico” Smith (SMAS/UMassD) for his editorial assistance. The authors also thank the two anonymous reviewers whose constructive comments led to a significant improvement of this manuscript.

References

- Alae, M., Ivey, G., Pattiaratchi, C., 2004. Secondary circulation induced by flow curvature and Coriolis effects around headlands and islands. *Ocean Dynamics* 54, 27–38.
- Berthot, A., Pattiaratchi, C., 2006. Field measurements of the three-dimensional current structure in the vicinity of a headland-associated linear sandbank. *Continental Shelf Research* 26, 295–317.
- Brown, W., Mastrocco-Marques, G., Yu, Z. Tidal eddy motions in the western Gulf of Maine, Part 1: primary flow structure. *Continental Shelf Research*, submitted for publication.
- Chen, C., Beardsley, R., Limeburner, R., 1995. Variability of currents in late spring in the northern Great South Channel. *Continental Shelf Research* 15, 451–473.
- Doglioli, A.M., Griffo, A., Magaldi, M.G., 2004. Numerical study of a coastal current on a steep slope in presence of a cape: the case of the Promontorio di Portofino. *Journal of Geophysical Research* 109, 19.
- Garrett, C., Loucks, R.H., 1976. Upwelling along the Yarmouth shore of Nova Scotia. *Journal of Fisheries Research Board of Canada* 33, 116–117.
- Geyer, W., 1993. Three-dimensional flow around headlands. *Journal of Geophysical Research* 98, 955–966.
- Hench, J.L., Leutich, R.A., 2003. Transient tidal circulation and momentum balance at a shallow inlet. *Journal of Physical Oceanography* 33, 913–932.
- Holboke, M., 1998. Variability of the Maine Coastal Current Under Spring Conditions. Ph.D. Thesis. Thayer School of Engineering, Dartmouth College.
- Jones, O., Simons, R., Jones, E., Harris, J., 2006. Influence of seabed slope and Coriolis effects on the development of sandbanks near headlands. *Journal of Geophysical Research* 111, 1–23.
- Kalkwijk, J.P.T., Booij, R., 1986. Adaptation of secondary flow in nearly horizontal flow. *Journal of Hydraulic Research* 24, 19–37.
- Lynch, D., Ip, J., Naimie, C., Werner, F., 1996. Comprehensive coastal circulation model with application to the Gulf of Maine. *Continental Shelf Research* 16, 875–906.
- Lynch, D., Naimie, C., 1992. The M_2 tide and its residual on the outer banks of the Gulf of Maine. *Journal of Physical Oceanography* 23, 2222–2253.
- Lynch, D., Werner, F., Greenberg, D., Loder, J., 1992. Diagnostic model for baroclinic, wind-driven and tidal circulation in shallow seas. *Continental Shelf Research* 12, 37–64.
- Moody, J.A., Butman, B., Beardsley, R., Boicourt, W., Brown, W., Daifuku, P., Irish, J., Mayer, D., Mofjeld, H., Petrie, B., Ramp, S., Smith, P., Wright, W., 1984. Atlas of Tidal Elevation and Current Observations on the Northeast American Continental Shelf and Slope. Technical Report 1611. U.S. Department of the Interior.
- Mukai, A., Westerink, R., Luettich, J., Mark, D., 2002. Eastcoast 2001, A Tidal Constituent Database for Western North Atlantic, Gulf of Mexico, and Caribbean Sea. Technical Report. Coastal and Hydraulics Laboratory, US Army Corps of Engineers <<http://www.unc.edu/ims/ccats/tides/tides.htm>>.
- Neill, S.P., Hashemi, R.M., Elliott, A.J., 2007. An enhanced depth-averaged tidal model for morphological studies in the presence of rotary currents. *Continental Shelf Research* 27, 82–102.
- Pingree, R., 1978. The formation of the Shambles and other banks by tidal stirring of the seas. *Journal of the Marine Biological Association of the United Kingdom* 58, 211–226.
- Smagorinsky, J., 1963. General circulation experiments with the primitive equations I. The basic experiment. *Monthly Weather Review* 91, 99–164.
- Stokesbury, K., Harris, B., Marino II, M., 2004. Estimation of sea scallop abundance using video survey in off-shore U.S. waters. *Journal of Shellfish Research* 23, 33–40.
- Vennell, R., Old, C., 2007. High resolution observations of the intensity of secondary circulation along a curved tidal channel. *Journal of Geophysical Research* 112, C11008. doi:10.1029/2006JC003764.
- White, L., Wolanski, E., 2008. Flow separation and vertical motions in a tidal flow interacting with shallow-water island. *Estuarine, Coastal and Shelf Science* 77, 457–467.
- Wolanski, E., Asaeda, T., Tanaka, A., Deleersnijder, E., 1996. Three-dimensional island wakes in the field, laboratory experiments and numerical models. *Continental Shelf Research* 16, 1437–1452.
- Wolanski, E., Hamner, W.M., 1988. Topographically controlled fronts in the ocean and their biological influence. *Science* 241, 177–181.